



## Analysis of the dynamics of ${}^7\text{Li}$ -induced fusion with ${}^{\text{nat}}\text{Zr}$ up to 44 MeV

Rinku Prajapat  and Moumita Maiti *Department of Physics, Indian Institute of Technology Roorkee, Roorkee 247667, Uttarakhand, India*

(Received 2 April 2020; accepted 2 June 2020; published 22 June 2020)

An experimental study on the fusion dynamics of the  ${}^7\text{Li}+{}^{\text{nat}}\text{Zr}$  reaction has been carried out within the 4.0 to 6.3 MeV/nucleon energy range by measuring cross sections of the populated residues with the help of  $\gamma$ -ray spectrometry. The equilibrium and pre-equilibrium reaction models have been used in the framework of EMPIRE3.2.2 to analyze the measured residual cross sections to shed light on the reaction mechanism involved in it. It indicates that the complete and incomplete fusion of  ${}^7\text{Li}$  contribute to the residual cross sections. Thus, the strength of incomplete fusion has been derived and is compared with other  ${}^7\text{Li}$ -induced reactions in the similar mass range. Further, coupled channel (CC) calculations have been carried out to understand the effect of couplings in the fusion process. It has been observed that the fusion cross section is suppressed in  ${}^7\text{Li}+{}^{\text{nat}}\text{Zr}$  reaction as compared to CC calculations far above the Coulomb barrier. The isomeric cross-section ratio has also been obtained from the measured cross sections of the isomeric pairs of  ${}^{93,95}\text{Tc}$  that describes the role of angular momentum and relative spins of the ground and isomeric states with the variation of bombarding energy.

DOI: [10.1103/PhysRevC.101.064620](https://doi.org/10.1103/PhysRevC.101.064620)

### I. INTRODUCTION

Exploration of charged-particle-induced reactions is essential to accomplish an array of goals, such as to probe the structure of nuclei, particularly far from the stability line, to study the fundamentals of nuclear collisions, and to measure the reaction rates both to understand nuclear astrophysics and in the field of applied nuclear science. Apart from this, a variety of nuclear reaction processes such as complete fusion (CF) and incomplete fusion (ICF), equilibrium (EQ) and pre-equilibrium (PEQ) emissions, fusion-fission, quasielastic and deep inelastic, occur depending upon the entrance channel parameters (mass, charge, energy, reaction time, and impact parameter) of the interacting partners. In heavy-ion collisions, the direct nuclear processes help to probe the breakup of the weakly bound projectiles or transfer of few nucleons between the colliding partners; and these direct processes compete with the compound nuclear process at  $\approx 10.5$  MeV/nucleon energy [1]. Further, fusion reactions with weakly bound nuclei are also imperative to understand the stellar reactions, particularly low-energy-capture cross sections of astrophysical relevance. Besides, the complete fusion of heavy ions is the only tool to synthesize the superheavy elements [2]. But because of the low binding of weakly bound stable or radioactive nuclei, the fusion cross section gets reduced, which may create difficulty in forming superheavy nuclei [3]. In the case of CF, projectile transfers its total angular momentum to the target within the limit of  $0 < l \leq l_{\text{crit}}$ , while partial angular momentum transfer occurs with  $l \geq l_{\text{crit}}$  in peripheral collisions and ICF process. Thus, the exploration of heavy-ion fusion reactions

is necessary to understand the dynamics of nuclear reactions around and above the Coulomb barrier.

Britt and Quinton reported the first experimental evidence of ICF [1], which described the high-energy  $\alpha$ -particle emission, predominantly in the forward direction, during the bombardment of  ${}^{12}\text{C}$ ,  ${}^{14}\text{N}$ , and  ${}^{16}\text{O}$  in the Au and Bi targets, respectively. The cluster structured weakly bound stable ( ${}^{6,7}\text{Li}$  and  ${}^9\text{Be}$ ) and unstable halo ( ${}^{11}\text{Li}$ ,  ${}^{7,11}\text{Be}$ , and  ${}^8\text{B}$ ) projectiles used to explore reaction dynamics usually have low binding energies, and they tend to break up into the respective cluster fragments. Thus, distinct reaction processes emerge in the reaction dynamics like CF-ICF, elastic or no-capture breakup (EBU), and transfer followed by a breakup. When the projectile completely fuses with a target (without rupture), that leads to the formation of compound nucleus (CN), known as direct complete fusion (DCF), whereas if all the fragments of a projectile (after breakup) fuse with a target, the process is known as sequential complete fusion (SCF). However, measurement of residues could hardly describe the occurrence of DCF and SCF since both the methods lead to the formation of the same CN. Likewise, if one of the fragments fuses with the target and others fly away, the process is called ICF; if the target captures none of those fragments, the mechanism is termed as EBU. These reaction processes are pictorially demonstrated in Fig. 1.

Enhancement in fusion cross sections of tightly and weakly bound nuclei-induced reactions were observed when compared with the estimation from one-dimensional barrier penetration model (1D-BPM) in the sub-barrier energy region [4–10]; however, suppression in the fusion cross section has also been reported in the above-barrier energy region, particularly for the weakly bound stable projectiles [7–9,11]. Contrary to this, no evidence of fusion suppression was recognized for the weakly and tightly bound projectile-induced

\*Corresponding author: [moumita.maiti@ph.iitr.ac.in](mailto:moumita.maiti@ph.iitr.ac.in)

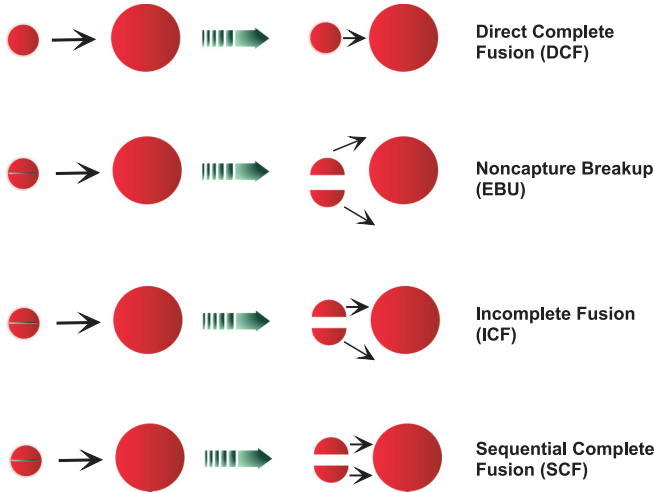


FIG. 1. A schematic diagram describes various fusion mechanisms of the loosely bound nuclei. It is a simplified version of the fusion procedures described in Ref. [11].

reactions on the light and medium-light mass targets [12,13]. In contrast, fusion cross sections at above-barrier energies were suppressed by  $\approx 20\text{--}35\%$  for the weakly bound projectile in the medium and light-heavy mass targets such as  ${}^6\text{Li}+{}^{90,96}\text{Zr}$ ,  ${}^{144}\text{Sm}$ ,  ${}^7\text{Li}+{}^{144,154}\text{Sm}$ ,  ${}^{159}\text{Tb}$ , and  ${}^9\text{Be}+{}^{89}\text{Y}$ ,  ${}^{144}\text{Sm}$  compared to the coupled-channel (CC) calculations without considering breakup and transfer couplings [7–9,14–17]. However, suppression in cross sections was  $\approx 30\text{--}40\%$  for the reactions with heavy mass targets at above-barrier energies,  ${}^{6,7}\text{Li}+{}^{209}\text{Bi}$  and  ${}^9\text{Be}+{}^{208}\text{Pb}$  [18]. Suppression in CF cross section may arise due to the following reasons:

- (i) A part of the incident flux gets lost because of the breakup of loosely bound projectiles;
- (ii) the rupture of projectiles yields the repulsive polarization potential that increases the barrier height and leads to the suppression in CF cross section near the barrier region [19]; and
- (iii) some of the residues might be stable or have short half-lives and hence they could not be measured by recoil-catcher activation techniques [20–24].

Moreover, Gasques *et al.* and Kumawat *et al.* [14,25] have demonstrated that CF suppression is independent of target charge ( $Z_T$ ) for the reactions involving loosely bound projectiles and light-medium, medium, and heavy mass targets ( ${}^{59}\text{Co}$ ,  ${}^{90,96}\text{Zr}$ ,  ${}^{144,154}\text{Sm}$ , and  ${}^{208}\text{Pb}$ ), contrary to Rath *et al.* [7], who described increase of CF suppression with increasing  $Z_T$ . It also increases with the decreasing breakup threshold ( $S_\alpha$ ) of the projectiles. The  $S_\alpha$  of the loosely bound nuclei having cluster structures [26] are 1.48, 2.45, and 1.57 MeV for  ${}^6\text{Li}(\alpha+d)$ ,  ${}^7\text{Li}(\alpha+t)$ , and  ${}^9\text{Be}(\alpha+\alpha+n)$ , respectively; hence, the breakup probability of  ${}^6\text{Li}$  is large compared to  ${}^7\text{Li}$  and  ${}^9\text{Be}$  nuclei. Thus, detailed knowledge of the dependency of CF suppression factor on the Coulombic charge of target and breakup threshold of the loosely bound projectile is still obligatory due to the discrepancies in the literature.

Various efforts have been made to understand the dynamics of heavy-ion collisions in the past few years. The direct or indirect signature of ICF over CF has been observed in the fusion of cluster-structured nuclei ( ${}^6,7\text{Li}$ ,  ${}^9\text{Be}$ ,  ${}^{12,13}\text{C}$ , and  ${}^{16}\text{O}$ ) around the Coulomb barrier. The dependence of different entrance channel parameters (incident energy, deformation parameter, and deformation length of the target) on ICF has been studied in the  $\alpha$ -emitting channels within  $\approx 3\text{--}10$  MeV/nucleon energy range [20,21,23–25,27]. The ICF strength fraction ( $F_{\text{ICF}}$ ) showed an increasing trend with the increasing charge of the target  $Z_T$  [28], while an indifferent nature of  $F_{\text{ICF}}$  against the target charge  $Z_T$  is reported in Ref. [29]. However, Giri *et al.* [27] concluded that  $F_{\text{ICF}}$  rises exponentially with entrance channel parameters such as mass asymmetry,  $Z_P Z_T$ , and  $\alpha$   $Q$  value of the projectile.

Besides this, the enhanced cross section for the inclusive  $\alpha$  production by breakup or transfer channels has been well established, and the competition between different breakup processes, such as direct and sequential breakup, and transfer channels has been studied with the help of continuum-discretized coupled channels (CDCC) for the reactions involving weakly bound projectiles with cluster structure [30–34]. It has been observed that the flux diverted from CF to ICF or transfer is mainly due to direct breakup components in the fusion of weakly bound projectiles [33]. Other processes like nucleon transfer followed by breakup have been demonstrated for  ${}^7\text{Li}$  projectiles that break up into  $\alpha+\alpha$  or  $\alpha+d$  after a proton pickup from the target or a neutron stripping from the projectile to target, along with the shell structure effect of the target nuclei [35,36]. However, it was suggested that the  $\alpha+\alpha$  channel from one proton pickup is less probable as compared to  $\alpha+d$  from one neutron stripping and  $\alpha+t$  (direct breakup) in  ${}^7\text{Li}+{}^{93}\text{Nb}$  system [36], while it was demonstrated that breakup of  ${}^7\text{Li}$  into  $\alpha+d$  is more favorable compared to the  $\alpha+t$  channel in the  ${}^7\text{Li}+{}^{65}\text{Cu}$  reaction [37]. We also made a systematic investigation of CF-ICF in  ${}^7\text{Li}+{}^{\text{nat}}\text{Mo}/{}^{93}\text{Nb}/{}^{89}\text{Y}$  within 3.5–7 MeV/nucleon energy range [20–23], along with some  ${}^7\text{Li}$ -,  ${}^9\text{Be}$ -,  ${}^{11}\text{B}$ -, and  ${}^{12}\text{C}$ -induced reactions in the medium mass targets to study EQ and PEQ reaction mechanisms in the past few years [38–47]. The contribution of PEQ emissions was also observed in the higher energy tail of the excitation functions, particularly in the  $3n$  channel [38,39].

Because of the discrepancies observed for the weakly bound projectile-mediated reactions, more experimental data are required to understand the phenomena of CF-ICF and dependency of fusion suppression, especially in light-medium and medium mass targets. This article reports a detailed study of the CF-ICF process and ICF strength fraction for the  ${}^7\text{Li}+{}^{\text{nat}}\text{Zr}$  system within the 4.0–6.3 MeV/nucleon energy range. Further, an analysis has been carried out to understand fusion suppression and its dependency on target charge in medium and light-heavy mass targets.

## II. EXPERIMENTAL DETAILS

The experiment was performed using the  ${}^7\text{Li}^{3+}$  beam delivered by the 14UD BARC-TIFR Pelletron facility, Mumbai, India, within the energy range 28–44 MeV in the laboratory frame for the  ${}^7\text{Li}+{}^{\text{nat}}\text{Zr}$  reaction. Self-supporting thin foils of

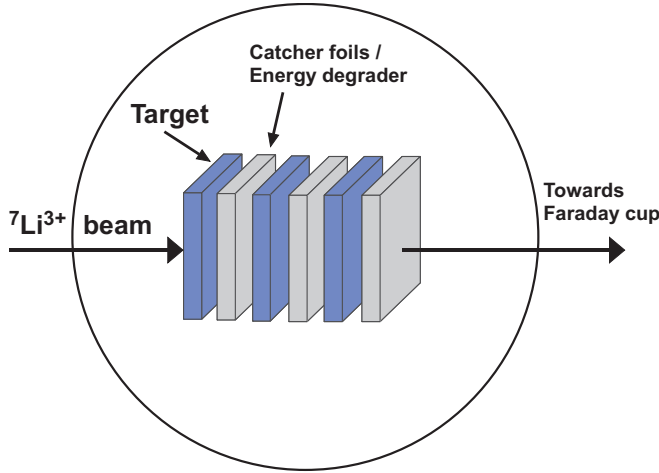


FIG. 2. A schematic diagram shows the target-catcher foil arrangement used for the study of  ${}^7\text{Li}$ -induced reaction on  ${}^{\text{nat}}\text{Zr}$ .

pure (99.99%) natural Zr and Al were prepared by the rolling method. The thickness of the Zr and Al foils were within 1.4–2.0 and 1.5–2.0  $\text{mg}/\text{cm}^2$ , respectively. A stack of two to three target foils was prepared by placing Al catcher foil behind each target. The purpose of the Al foils was to catch the recoiled residues in the forward beam direction and also for the energy degradation so that a suitable energy separation between the successive target foils could be attained. A total of five such target stacks were irradiated in this experiment by varying the bombarding energy so that some overlapping energy points be obtained between the two consecutive irradiations. The beam irradiation time was decided considering the projectile flux and half-lives of the expected residues. A constant beam current, which was typically in the range of  $\approx 15$  pA, was maintained throughout the experiment, and the amount of integral charge in each irradiation was measured by an electron-suppressed Faraday cup installed behind the target stack. A schematic diagram of the stack-foil arrangement has been shown in Fig. 2. The energy degradation of the  ${}^7\text{Li}$  ions in each foil of a stack was estimated using the Monte Carlo simulation-based SRIM (the stopping and range of the ions in the matter) code [48]. The projectile energy at a particular target is the average of the incident and outgoing energy.

After the end of bombardment (EOB), populated residues in each target-catcher assembly (Zr-Al) were identified with the help of  $\gamma$ -ray spectroscopy following the characteristics  $\gamma$  rays and decay profile using a large-volume high-purity germanium detector and the GENIE-2K software. The detector was precalibrated with the help of conventional sources  ${}^{137}\text{Cs}$  (30.08 y),  ${}^{152}\text{Eu}$  (13.517 y), and  ${}^{60}\text{Co}$  (5.27 y) of known activity. The resolution of detector was 2.0 keV at 1332-keV  $\gamma$  rays of  ${}^{60}\text{Co}$ . The spectroscopic data of the residues are tabulated in Table I. The yield ( $Y_i$ ) of the  $i$ th residue at the EOB is measured by

$$Y_i = \frac{C(t_c)}{\theta_i^\gamma \epsilon_i^\gamma} e^{\lambda_i t_w}. \quad (1)$$

The characteristic  $\gamma$  rays have been used to measure the cross section of the  $i$ th residue at the energy  $E$  using the following

TABLE I. Nuclear spectroscopic data [61] of the residues produced in  ${}^7\text{Li}+{}^{\text{nat}}\text{Zr}$  reaction. The  $\gamma$ -ray energies marked in bold are used for cross-section calculation.

Residue	$J^\pi$	$T_{1/2}$	Decay mode (%)	$E_\gamma$ (keV)	$I_\gamma$ (%)
${}^{96}\text{Tc}$	$7^+$	4.28 d	$\epsilon + \beta^+$ (100)	778.22	99.76
				<b>812.54</b>	82.0
${}^{95}\text{Tc}$	$9/2^+$	20.0 h	$\epsilon + \beta^+$ (100),	<b>765.79</b>	93.8
				<b>1073.71</b>	3.74
${}^{95m}\text{Tc}$	$1/2^-$	61 d	$\epsilon + \beta^+$ (96.12), IT <sup>a</sup> (3.88)	<b>204.12</b>	63.2
				582.08	30.0
				835.15	26.6
${}^{94}\text{Tc}$	$7^+$	4.88 h	$\epsilon^b + \beta^+$ (100)	<b>702.67</b>	99.6
				871.05	99.9
${}^{94m}\text{Tc}$	$2^+$	52 min	$\epsilon + \beta^+$ (100), IT < (0.10)	871.05	94.2
${}^{93}\text{Tc}$	$9/2^+$	2.75 h	$\epsilon + \beta^+$ (100)	<b>1362.94</b>	66.2
				<b>1520.28</b>	24.4
${}^{93m}\text{Tc}$	$1/2^-$	43.5 min	IT (77.4), $\epsilon + \beta^+$ (22.6)	<b>391.83</b>	58.3
${}^{93m}\text{Mo}$	$21/2^+$	6.85 h	IT (99.88), $\epsilon + \beta^+$ (0.12)	<b>263.05</b>	57.4
				684.69	99.9
				1477.14	99.1
${}^{96}\text{Nb}$	$6^+$	23.35 h	$\beta^-$ (100)	<b>568.87</b>	58.0
				778.22	96.45
				1091.35	48.5
${}^{90}\text{Nb}$	$8^+$	14.6 h	$\epsilon + \beta^+$ (100)	<b>141.18</b>	66.8
				<b>1129.22</b>	92.7
				2318.96	82.0

<sup>a</sup>Isomeric transition.

<sup>b</sup>Electron capture.

activation relation:

$$\sigma_i(E) = \frac{Y_i}{\rho_{tg} \phi (1 - e^{-\lambda_i t_r})}, \quad (2)$$

where  $C(t_c)$  is the count rate (counts per second) under the photopeak,  $\theta_i^\gamma$  and  $\epsilon_i^\gamma$  are the branching intensity of characteristic  $\gamma$ -ray and geometry-dependent efficiency of the detector,  $\lambda_i$  is the disintegration constant,  $\rho_{tg}$  is the areal density of target nuclei, and incident beam flux is  $\phi$ . The counting time, irradiated time, and the waiting time between the EOB and measurement are denoted by  $t_c$ ,  $t_r$ , and  $t_w$ , respectively. The uncertainty in the cross-section measurement is considered from the following sources: (i) nonuniformity in the target thickness was maximum 2%, (ii) inaccuracy in the measurement of efficiency of the detector was  $\leq 2\%$ , (iii) propagation of error due to the incident beam flux was estimated maximum as 7%, (iv) statistical error in the peak area count has been considered, and (v) there might be some error in energy due to the beam energy degradation in the successive target-catcher foils. However, energy straggling in the target-catcher was expected to be very small [49,50]; hence it is neglected in the present case. The average estimated error was found to be  $\approx 12\%$  considering all those factors, except for a few cases where it is estimated as  $\approx 18\%$ . The residual cross section data are presented here with a 95% confidence level.

### III. THEORETICAL CALCULATION

The nuclear reaction model code EMPIRE3.2.2 [51] has been used for the estimation of the cross section of the residues from  ${}^7\text{Li}+{}^{\text{nat}}\text{Zr}$  reaction. EMPIRE has been designed

to study comprehensive aspects of theoretical models over a broad range of energy and projectiles such as photons, nucleons, deuterons, tritons,  $^3\text{He}$ ,  $\alpha$  particles, and other heavy ions; however, EMPIRE is more reliable for the study of heavy-ion-induced reactions. It accounts for the three dominant reaction processes: direct, PEQ, and EQ or the compound nuclear (CN) reaction in its frame of reference. The direct reactions are predicted using the coupled channel (CC) approach and distorted-wave Born approximation (DWBA) [52]. The CC method is appealing to study the elastic scattering channel and low-lying states, which are strongly excited in inelastic scattering for deformed nuclei, while the DWBA is commonly used for the inelastic scattering, for both strongly and weakly coupled levels, and it is valid for small deformation. However, the simplified coupled-channel approach (CCFUS) [53] has been used in EMPIRE for the estimation of heavy-ion fusion that incorporates the inelastic excitations and transfers reaction channels independently that couple to the initial ground state. The PEQ emission that occurs due to the localized high-energy density has been incorporated through the quantum-mechanical and phenomenological models. The quantum mechanical PEQ models are based on the multistep direct (MSD) and multistep compound (MSC) theory [54,55], while phenomenological models are the exciton model (EM) and Monte Carlo pre-equilibrium code. However, the understanding of PEQ reactions for the heavy projectiles still lacks in the quantum mechanical models; hence they are not popularly used. EMPIRE uses an input library based on RIPL-3 [56] that covers nuclear masses, optical model parameters, ground-state deformations, discrete levels and decay schemes, level densities, fission barriers, and  $\gamma$ -ray strength functions. In the present calculation, EM and Hauser-Feshbach (HF) formalism have been used for the estimation of PEQ, and EQ cross sections of the residues with width fluctuation correction, which is necessary to establish a correlation between the incident and exit channels, respectively.

Three phenomenological nuclear level density models, such as Gilbert-Cameron model (GCM) [57], generalized super-fluid model (GSM) [58], and enhanced generalized superfluid model (EGSM) [59] with mean free path parameter of 1.5 (optimum value), have been used to estimate the residual cross sections. The GC model adopts constant temperature formalism at the low excitation energies; however, beyond a particular matching point (say  $U_x$ ), the Fermi gas (FG) formula has been considered. The GSM accounts for the phase transition from a superfluid to normal behavior at low energy to the locality of high energy, which is characterized by the FG model. On the other hand, the EGSM adopts the superfluid model below the critical excitation energy and FG model above it. The angular momentum is treated more accurately in EGSM, which is favorable for heavy-ion-induced reactions.

In the case of the HF model, the cross section of a ( $\alpha$ ,  $\beta$ ) reaction can be obtained from

$$\sigma_{\alpha,\beta}(E) = \sum_{J^\pi} \sigma_{\alpha}^{\text{CN}}(E, J^\pi) \frac{T_{\beta}(E_x, J^\pi)}{\sum_{\gamma} T_{\gamma}(E_x, J^\pi)}, \quad (3)$$

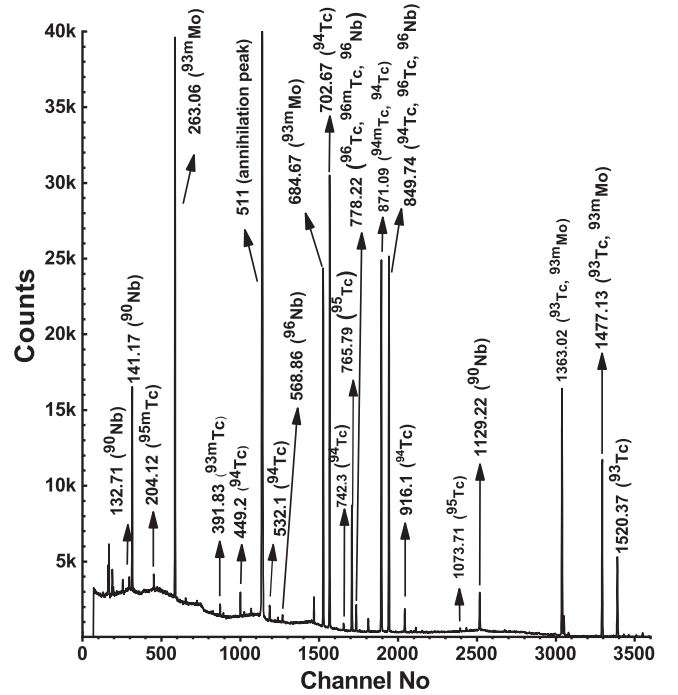


FIG. 3. A typical  $\gamma$ -ray spectrum of the 42.0-MeV  $^7\text{Li}$  irradiated  $^{\text{nat}}\text{Zr}$  target collected 61.6 min after the EOB. The  $\gamma$ -ray energies, shown in the spectrum, are in keV.

where  $\sigma_{\alpha}^{\text{CN}}(E, J^\pi)$  represents the compound nucleus formation cross section in a state of spin and parity  $J^\pi$  and the second part of Eq. (3) is the decay probability in terms of transmission coefficients. On the other hand, the differential cross section of PEQ emission can be calculated from

$$\frac{d\sigma_{\alpha,\beta}}{d\epsilon_{\beta}} = \sigma_{\alpha,\beta}^{\text{reac}}(E) \Delta_{\alpha,\beta}(E) \sum_n W_{\beta}(E_x, n, \epsilon_{\beta}) \tau(n), \quad (4)$$

where  $\sigma_{\alpha,\beta}^{\text{reac}}$  represents the cross section of the reaction ( $\alpha$ ,  $\beta$ ) and  $W_{\beta}(E_x, n, \epsilon_{\beta})$  is the emission probability of particle type  $\beta$  (or  $\gamma$  rays) with energy  $\epsilon_{\beta}$  from a state with  $n$  excitons with excitation energy  $E_x$  of CN.  $\Delta_{\alpha,\beta}(E)$  is the depletion factor and defined with direct reaction cross section  $\sigma_{\alpha,\beta}^{\text{dir}}$  as

$$\Delta_{\alpha,\beta}(E) = 1 - \frac{\sigma_{\alpha,\beta}^{\text{dir}}(E)}{\sigma_{\alpha,\beta}^{\text{reac}}(E)}. \quad (5)$$

This depletion factor incorporates the flux loss as a result of direct reaction processes.

#### IV. RESULTS AND DISCUSSION

The complete or partial fusion of  $^7\text{Li}$  in  $^{\text{nat}}\text{Zr}$  has led to the production of  $^{93,93m,94,95,95m,96}\text{Tc}$ ,  $^{93m}\text{Mo}$ , and  $^{90,96}\text{Nb}$  radionuclides. A typical  $\gamma$ -ray spectrum of the 42.0-MeV  $^7\text{Li}$  irradiated  $^{\text{nat}}\text{Zr}$ , collected 61.6 min after the EOB, is presented in Fig. 3. The background-subtracted peak area of all the unique characteristic  $\gamma$  rays of each radionuclide was analyzed to measure activity and hence residual cross section from Eq. (2). The cross sections of residues measured from



TABLE II. The measured cross sections of the residues are tabulated at various incident energies.

Energy (MeV)	Cross section (mb)								
	$^{96}\text{Tc}$	$^{95m}\text{Tc}$	$^{95}\text{Tc}$	$^{94}\text{Tc}$	$^{93m}\text{Tc}$	$^{93}\text{Tc}$	$^{93m}\text{Mo}$	$^{96}\text{Nb}$	$^{90}\text{Nb}$
$28.7 \pm 0.6$	$161.9 \pm 17.7$	$30.6 \pm 4.9$	$184.3 \pm 18.7$	$320.9 \pm 30.0$	$0.0 \pm 0.0$	$8.1 \pm 1.0$	$2.8 \pm 0.4$	$20.1 \pm 2.4$	$7.7 \pm 0.9$
$30.5 \pm 0.6$	$159.6 \pm 19.2$	$32.7 \pm 5.3$	$206.6 \pm 32.0$	$330.3 \pm 35.5$	$3.3 \pm 0.6$	$23.6 \pm 2.4$	$10.1 \pm 1.2$	$20.8 \pm 2.5$	$10.8 \pm 1.2$
$32.0 \pm 0.5$	$103.7 \pm 11.3$	$25.8 \pm 4.6$	$177.4 \pm 19.8$	$341.1 \pm 31.9$	$3.0 \pm 0.5$	$57.7 \pm 6.0$	$19.4 \pm 2.1$	$13.8 \pm 2.0$	$12.2 \pm 1.5$
$33.4 \pm 0.5$	$90.8 \pm 10.4$	$23.8 \pm 4.2$	$185.0 \pm 21.1$	$328.1 \pm 30.9$	$3.9 \pm 0.6$	$87.1 \pm 8.9$	$31.7 \pm 3.4$	$14.0 \pm 2.1$	$13.8 \pm 1.7$
$34.8 \pm 0.5$	$76.5 \pm 9.1$	$20.9 \pm 4.0$	$184.7 \pm 20.4$	$303.0 \pm 28.6$	$5.5 \pm 0.7$	$115.8 \pm 11.7$	$48.7 \pm 5.0$	$13.3 \pm 1.8$	$18.1 \pm 2.2$
$38.3 \pm 0.5$	$68.4 \pm 8.3$	$20.2 \pm 2.7$	$180.2 \pm 19.5$	$247.5 \pm 23.5$	$6.8 \pm 1.0$	$176.2 \pm 17.4$	$100.8 \pm 10.0$	$13.8 \pm 2.1$	$29.0 \pm 3.2$
$39.6 \pm 0.5$	$61.0 \pm 7.4$	$17.6 \pm 2.7$	$167.1 \pm 19.7$	$192.1 \pm 18.2$	$5.6 \pm 0.8$	$176.2 \pm 17.3$	$107.5 \pm 10.7$	$13.0 \pm 2.2$	$32.0 \pm 3.6$
$40.8 \pm 0.5$	$69.3 \pm 9.0$	$17.6 \pm 2.7$	$162.8 \pm 19.7$	$198.5 \pm 18.8$	$6.6 \pm 1.0$	$202.7 \pm 20.1$	$140.4 \pm 13.7$	$13.5 \pm 2.0$	$43.6 \pm 4.6$
$42.0 \pm 0.5$	$80.2 \pm 9.5$	$15.4 \pm 2.4$	$157.0 \pm 24.8$	$193.3 \pm 18.3$	$5.3 \pm 0.7$	$212.2 \pm 20.9$	$152.6 \pm 15.0$	$13.9 \pm 2.1$	$50.3 \pm 5.4$
$43.3 \pm 0.5$	$99.1 \pm 11.9$	$19.0 \pm 2.8$	$156.7 \pm 19.2$	$185.2 \pm 17.7$	$6.1 \pm 0.9$	$244.2 \pm 24.1$	$187.1 \pm 18.1$	$14.6 \pm 2.2$	$67.3 \pm 7.0$

the  $^7\text{Li} + \text{natZr}$  reaction up to 44 MeV, in the present study, are listed in Table II. The measured cross sections of residues have been compared with theoretical predictions of EMP3.2.2 with different level densities, as depicted in Fig. 4. The CF

and ICF cross sections, the variation of ICF strength fraction ( $F_{\text{ICF}}$ ), are presented in Figs. 5 and 6 against incident energy. Experimental data are shown by symbols with uncertainty, while lines denote theoretical predictions.

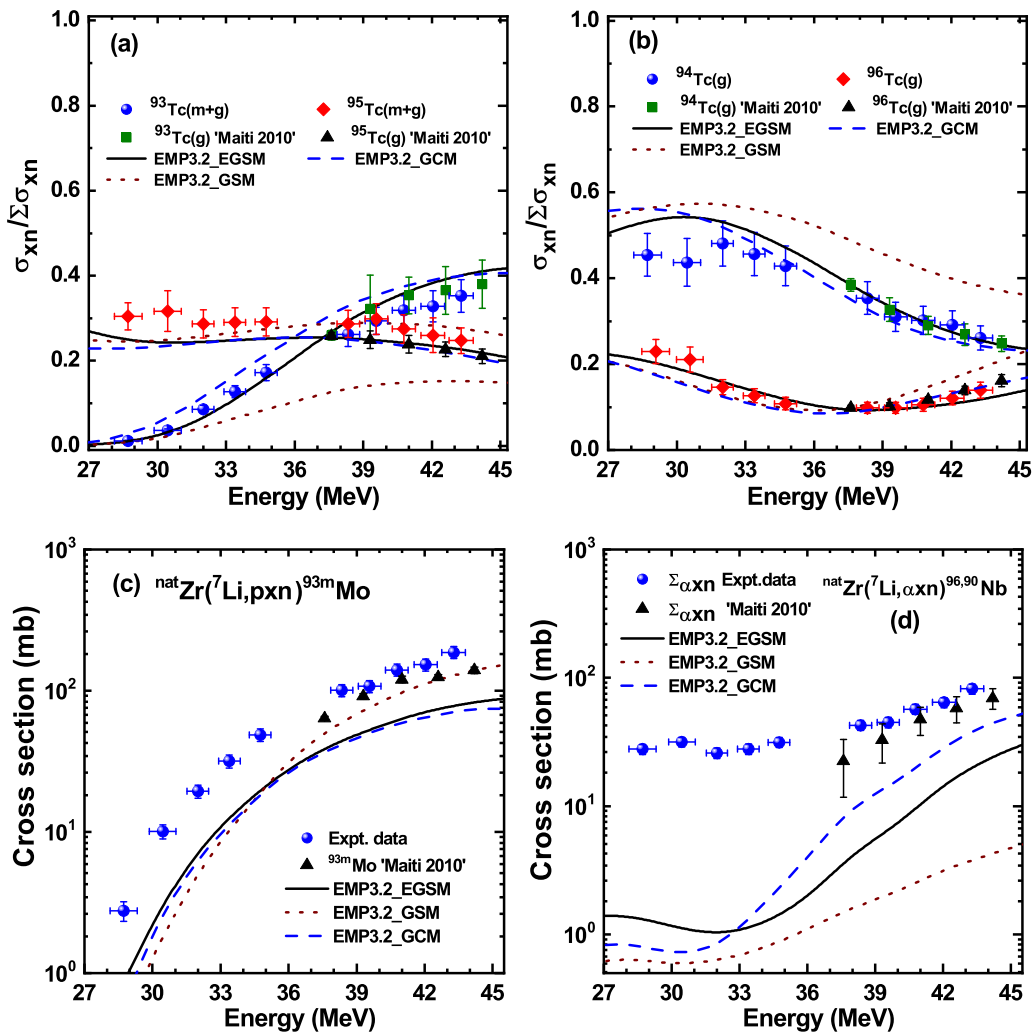


FIG. 4. Comparison between the measured ratio of the individual channel ( $xn$ ) to the sum of all such channels ( $\sum \sigma_{xn}$ ) of (a)  $^{93,95}\text{Tc}(m+g)$  and  $^{93,95}\text{Tc}(g)$  [42], (b)  $^{94,96}\text{Tc}(g)$  and  $^{94,96}\text{Tc}(g)$  [42], with predicted ratios from EMP3.2, [(c), (d)] represent the comparison between the excitation function of  $^{93m}\text{Mo}$ ,  $^{93m}\text{Mo}$  [42] and  $^{90,96}\text{Nb}$ ,  $^{90,96}\text{Nb}$  [42] with theoretical predictions of EMP3.2 (denoted as EMP3.2), respectively.

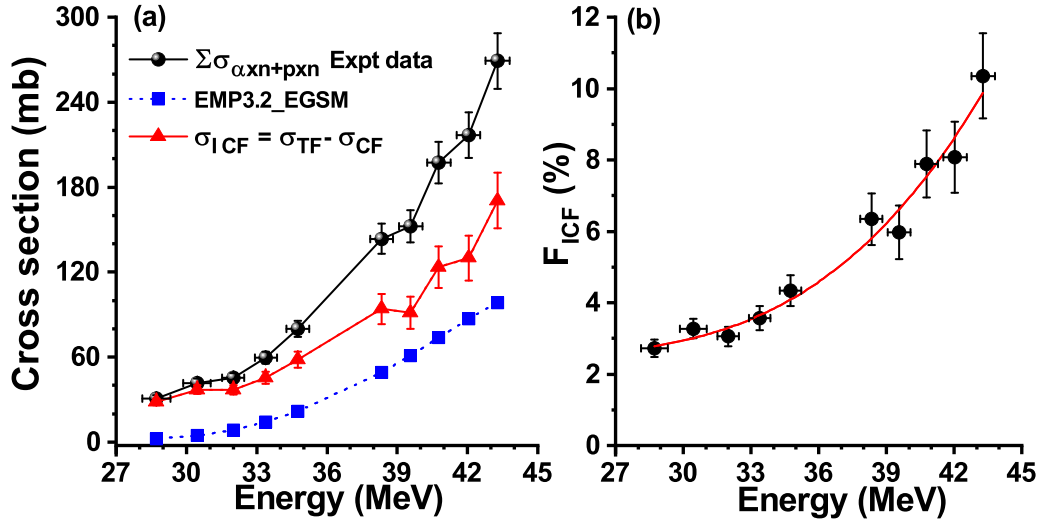


FIG. 5. Variation of (a) CF and ICF cross section ( $\Sigma \sigma_{\alpha xn + pxn}$ ) for  $\alpha xn + pxn$  channel, and (b) ICF strength fraction (fitted line is to guide the eye), with projectile energy.

### A. Analysis of residual cross sections

The measured excitation function of residues produced in  ${}^7\text{Li} + {}^{\text{nat}}\text{Zr}$  reaction has been compared with EMPIRE estimations, where weighted averages of cross sections from all the abundant isotopes of Zr,  ${}^{90}\text{Zr}$  (51.45%),  ${}^{91}\text{Zr}$  (11.22%),  ${}^{92}\text{Zr}$  (17.15%),  ${}^{94}\text{Zr}$  (17.38%), and  ${}^{96}\text{Zr}$  (2.8%), have been considered.

Because of the existence of five naturally abundant isotopes of  ${}^{\text{nat}}\text{Zr}$ , various reaction channels may contribute to the production of a single residue. Figures 4(a) and 4(b) compare measured fractional cross sections of  ${}^{93}\text{Tc}(m+g)$  and  ${}^{95}\text{Tc}(m+g)$  and of  ${}^{94}\text{Tc}(g)$  and  ${}^{96}\text{Tc}(g)$ , respectively, with the theoretical predictions. The fractional cross section is defined as the ratio of a particular residue cross section that is

populated by the  $xn$  channel ( $\sigma_{\text{res}}$ ) to the sum of cross sections of all residues produced through the  $xn$  channel ( $\Sigma \sigma_{\text{res}}$ ) at a particular energy. The production of the  $xn$  channel residues comes purely from the CF of  ${}^7\text{Li}$  in  ${}^{\text{nat}}\text{Zr}$ . The fractional cross sections,  $\sigma_{\text{res}}/\Sigma \sigma_{\text{res}}(xn)$ , estimated from EMPIRE with EGSM and GCM level density are in good agreement with the experimental ratios, but GSM calculations underestimate and overestimate the measured data of  ${}^{93}\text{Tc}(m+g)$  and  ${}^{94g}\text{Tc}$ , respectively, throughout the energy range. A critical observation demonstrates that EMPIRE with the EGSM level density best reproduces the measured cross sections of Tc residues produced via the  $xn$  channel. The residues  ${}^{93m}\text{Mo}$  and  ${}^{90,96}\text{Nb}$  have enhanced cross sections as compared to EMPIRE throughout the energy range, except for  ${}^{93m}\text{Mo}$  beyond 42-MeV energy, where GSM level density reproduces the measured data reported by Maiti *et al.* [42], as depicted in Figs. 4(c) and 4(d). It is worth mentioning here that the same set of input parameters, which reproduced the measured  $xn$  channel cross sections satisfactorily, has been used to estimate cross sections of the residues  ${}^{93m}\text{Mo}$  and  ${}^{90,96}\text{Nb}$  in the framework of EMPIRE with EGSM level density model. The statistical model code EMPIRE assumes CF of the projectile, and energy relaxation of the composite system evolves through the direct, PEQ, and EQ reactions; hence, it is evident that the observed enhancement in the production cross sections of  ${}^{93m}\text{Mo}$  and  ${}^{90,96}\text{Nb}$  is due to a process that goes unaccounted in the EMPIRE calculation. The enhanced cross section could be attributed to the ICF process, as the probability of occurrence of breakup phenomena is established for weakly bound  ${}^7\text{Li}$  in the literature [20,21,35,36,60]. Thus, the production of  ${}^{93m}\text{Mo}$  and  ${}^{90,96}\text{Nb}$  is contributed by both CF (via  $xn$ ,  $pxn$ , and  $\alpha xn$  channels) and ICF processes. Similar enhancement in the  ${}^{93m}\text{Mo}$  and  ${}^{90,96}\text{Nb}$  cross sections was observed by Maiti *et al.* [42] in the energy range  $\approx 37$ –45 MeV, as depicted in Figs. 4(c) and 4(d).

The large production cross section observed for  ${}^{93m}\text{Mo}$  and  ${}^{90,96}\text{Nb}$ , above the theoretical estimate, in the present experiment could be attributed to the following:

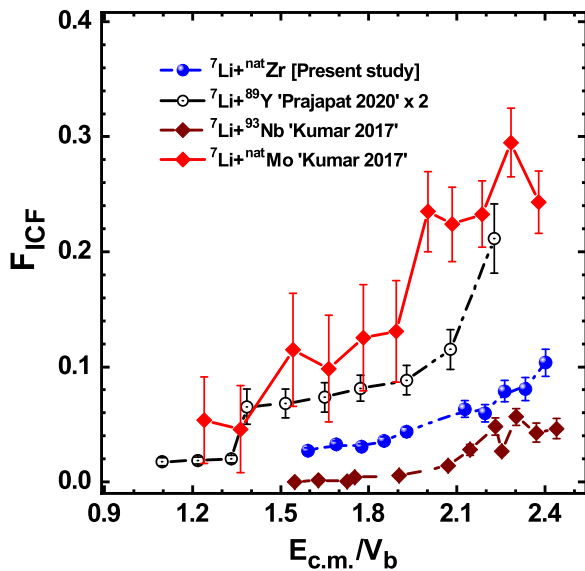


FIG. 6. ICF strength fraction ( $F_{ICF}$ ) plotted as a function of reduced projectile energy ( $E_{c.m.}/V_b$ ) for  ${}^7\text{Li} + {}^{\text{nat}}\text{Zr}$  (present work),  ${}^7\text{Li} + {}^{89}\text{Y}$  [23],  ${}^7\text{Li} + {}^{93}\text{Nb}$  [21], and  ${}^7\text{Li} + {}^{\text{nat}}\text{Mo}$  [20] systems.

TABLE III. Probable CF and ICF reactions, corresponding  $Q$  values, and threshold ( $E_{\text{th}}$ ) are listed below.

CF of ${}^7\text{Li}$			ICF of ${}^7\text{Li}$ ( ${}^7\text{Li} \rightarrow \alpha+t$ )		
Reaction	$Q$ value	$E_{\text{th}}$	Reaction	$Q$ value	$E_{\text{th}}$
${}^{90}\text{Zr}({}^7\text{Li}, p3n){}^{93m}\text{Mo}$	-18.56	20.0	${}^{90}\text{Zr}(\alpha, n){}^{93m}\text{Mo}$	-7.61	7.95
${}^{90}\text{Zr}({}^7\text{Li}, 5n2p){}^{90}\text{Nb}$	-46.14	49.74	${}^{90}\text{Zr}(\alpha, p3n){}^{90}\text{Nb}$	-35.19	36.76
${}^{90}\text{Zr}({}^7\text{Li}, \alpha3n){}^{90}\text{Nb}$	-17.84	19.24	${}^{91}\text{Zr}(\alpha, 2n){}^{93m}\text{Mo}$	-14.81	15.46
${}^{91}\text{Zr}({}^7\text{Li}, p4n){}^{93m}\text{Mo}$	-25.75	27.74	${}^{91}\text{Zr}(\alpha, p4n){}^{90}\text{Nb}$	-42.38	44.25
${}^{91}\text{Zr}({}^7\text{Li}, \alpha4n){}^{90}\text{Nb}$	-25.04	26.97	${}^{92}\text{Zr}(\alpha, 3n){}^{93m}\text{Mo}$	-23.44	24.46
${}^{91}\text{Zr}({}^7\text{Li}, 2p){}^{96}\text{Nb}$	-1.96	2.12	${}^{92}\text{Zr}(\alpha, p5n){}^{90}\text{Nb}$	-51.02	53.24
${}^{92}\text{Zr}({}^7\text{Li}, p5n){}^{93m}\text{Mo}$	-34.39	37.02	${}^{94}\text{Zr}(\alpha, 5n){}^{93m}\text{Mo}$	-38.39	40.03
${}^{92}\text{Zr}({}^7\text{Li}, \alpha5n){}^{90}\text{Nb}$	-33.67	36.24	${}^{94}\text{Zr}(\alpha, pn){}^{96}\text{Nb}$	-14.60	15.22
${}^{92}\text{Zr}({}^7\text{Li}, 2pn){}^{96}\text{Nb}$	-10.60	11.41	${}^{96}\text{Zr}(\alpha, p3n){}^{96}\text{Nb}$	-28.91	30.12
${}^{94}\text{Zr}({}^7\text{Li}, \alpha n){}^{96}\text{Nb}$	2.74	0.0	${}^{90}\text{Zr}(t, 3n){}^{90}\text{Nb}$	-15.38	15.89
${}^{96}\text{Zr}({}^7\text{Li}, \alpha3n){}^{96}\text{Nb}$	-11.57	12.41	${}^{91}\text{Zr}(t, 4n){}^{90}\text{Nb}$	-22.57	23.32
			${}^{92}\text{Zr}(t, 5n){}^{90}\text{Nb}$	-31.20	32.23
			${}^{94}\text{Zr}(t, n){}^{96}\text{Nb}$	5.21	0.0
			${}^{96}\text{Zr}(t, 3n){}^{96}\text{Nb}$	-9.10	9.39
			${}^{91}\text{Zr}(d, 3n){}^{90}\text{Nb}$	-16.31	16.67

(1) CF: Complete fusion of  ${}^7\text{Li}$  in one of the naturally abundant isotopes of  ${}^{\text{nat}}\text{Zr}$ , i.e.,  ${}^{90,91,92,94,96}\text{Zr}$  isotopes, may lead to the formation of a compound nucleus (CN), which eventually decay via  $xn$ ,  $pxn$ , and  $\alpha xn$  channels to form  ${}^{93m}\text{Mo}$  and  ${}^{90,96}\text{Nb}$ , respectively. The possible reactions, which may contribute to the production of those residues via CF mechanism, are listed in Table III.

(2) ICF: Being weakly bound,  ${}^7\text{Li}$  may break up into its constituent fragments ( ${}^7\text{Li} \rightarrow \alpha+t$ ), and fusion of one of these fragments in the target nucleus would form a reduced CN, and remaining fragment flies away in the forward direction (known as a spectator). The following ICF processes may contribute to the large production of  ${}^{93m}\text{Mo}$  and  ${}^{90,96}\text{Nb}$  in the  ${}^7\text{Li}+{}^{\text{nat}}\text{Zr}$  reaction.

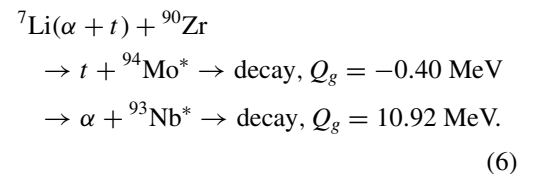
(a) In the case of ICF of  ${}^7\text{Li}$ , the fusion of an  $\alpha$  particle with  ${}^{90}\text{Zr}$ , the highest abundant Zr isotope, leads to formation of an excited CN  ${}^{94}\text{Mo}^*$ , which could eventually emit a  $n$  and  $p+3n$  to form the residues  ${}^{93m}\text{Mo}$  and  ${}^{90}\text{Nb}$ , respectively, and  $t$  moves in the forward direction as a spectator. Similarly, the fusion of  $t$  in  ${}^{90}\text{Zr}$  leads to formation of  ${}^{90}\text{Nb}$  by emitting  $3n$  from the CN  ${}^{93}\text{Nb}^*$ , and the  $\alpha$  particle moves as a spectator. However, production of  ${}^{90}\text{Nb}$  and  ${}^{96}\text{Nb}$  is more likely through the fusion of  $t$ , due to low reaction threshold compared to the fusion of the  $\alpha$  particle. The assumed participation of the abundant isotopes of  ${}^{\text{nat}}\text{Zr}$  in this regard are listed in Table III along with the  $Q$  value.

(b) One neutron stripping from  ${}^7\text{Li}$  in the field of target nucleus, say  ${}^{90}\text{Zr}$ , leads to the formation of  ${}^{91}\text{Zr}$  and  ${}^6\text{Li}$  ( ${}^7\text{Li}+{}^{90}\text{Zr} \rightarrow {}^6\text{Li}+{}^{91}\text{Zr}$ ). Weakly bound  ${}^6\text{Li}$  may dissociate into  $\alpha+d$ ; the fusion of any one of the breakup fragments ( $\alpha$  or  $d$ ) with the isotopes of  ${}^{\text{nat}}\text{Zr}$  would lead to the formation of  ${}^{93m}\text{Mo}$  and  ${}^{90,96}\text{Nb}$  through the emission of light

particles, and the other fragment would move in the forward direction as a spectator. There might be a chance of direct  $\alpha$  or  $d$  transfer, as explained in Ref. [30]; however, its possibility will depend on the optimum  $Q$  value and ground-state  $Q$  value of the reaction.

(c) One-proton pickup by  ${}^7\text{Li}$  from the target forms an unstable  ${}^8\text{Be}$ , which possibly breaks up into two  $\alpha$  particles ( ${}^8\text{Be} \rightarrow \alpha+\alpha$ ) and isotopes of Y, including stable  ${}^{89}\text{Y}$ , as heavy residue; if any one of the  $\alpha$  particles fuses with  ${}^{\text{nat}}\text{Zr}$  isotopes, it will lead to the production of  ${}^{93m}\text{Mo}$  and  ${}^{90,96}\text{Nb}$ , as shown in Table III, while the unfused  $\alpha$  particle would fly in the forward direction with its initial velocity. The optimum  $Q$  value for the one proton pickup by  ${}^7\text{Li}$ , say for the  ${}^7\text{Li}+{}^{\text{nat}}\text{Zr}$  reaction, is comparable with the ground-state  $Q$  value of the reaction within the incident energy range; therefore, one-proton pickup is possible in this system. The probability of fusion of a  $\alpha$ -particle in Y isotopes would be negligible.

(d) Possibility of direct transfer of the breakup fragments ( $\alpha$  or  $t$ ) from the ground state of  ${}^7\text{Li}$  to the target should not be ignored. However, optimum  $Q$  values would suggest the preferential population of high-lying states in regions where little or nothing is known about the structure of the relevant nuclei. In the present scenario, let us consider the  ${}^7\text{Li}+{}^{90}\text{Zr}$  reaction, the direct transfer of  $\alpha$  or  $t$  to the  ${}^{90}\text{Zr}$ , and the subsequent decay of the product is shown in Eq. (6):



However, subsequent  $Q$  optimum values for the direct  $\alpha$  or  $t$  transfer in  ${}^7\text{Li}+{}^{90}\text{Zr}$  reaction does not match with their respective ground-state  $Q$  values within the studied energy range. Hence, the direct transfer of  $\alpha$  or  $t$  may not be feasible in this reaction; however, it is tough to separate breakup followed by the capture of one of the fragments (refer to Table III) from a transfer process, while both forming the same nucleus.

Since the present experiment has been performed using the stack-foil technique and inclusive  $\gamma$ -ray spectrometric method, it restricts to disentangle different breakup or transfer mechanisms from other reaction processes.

### B. Analysis of ICF

The enhancement in the measured cross sections of residues  ${}^{93m}\text{Mo}$  and  ${}^{90,96}\text{Nb}$ , produced through the  $pxn$  and  $\alpha xn$  channels, respectively, has been observed as compared to the EMPIRE estimate, which does not account for projectile breakup or ICF mechanism in its calculation. However, measured cross sections of the  ${}^{93,94,95,96}\text{Tc}$  residues populated through the  $xn$  channels are well reproduced by EMPIRE with the same set of input parameters. Thus, enhanced residual cross sections of  ${}^{93m}\text{Mo}$  and  ${}^{90,96}\text{Nb}$  are assumed due to ICF of  ${}^7\text{Li}$  in the Zr target, as the breakup phenomena of weakly bound  ${}^6,7\text{Li}$  in the nuclear field is already established [11,20,21,23,30–36,60].

Since the enhancement in  $pxn$  and  $\alpha xn$ -channel cross sections is attributed to ICF, for better insight, the relative strengths of ICF in the  $\alpha$ - and  $p$ -emitting channels have been analyzed with the help of the data reduction method [17,20,24] considering the EMPIRE estimate with EGSM level density as reference.  $\sum \sigma_{\text{ICF}}^{\alpha xn+pxn} = \sum \sigma_{\text{TF}}^{\alpha xn+pxn} - \sum \sigma_{\text{CF}}^{\alpha xn+pxn}$  for the  ${}^7\text{Li}+{}^{\text{nat}}\text{Zr}$  reaction, where  $\sum \sigma_{\text{TF}}$  and  $\sum \sigma_{\text{CF}}$  are the sum of measured cross sections of  ${}^{93m}\text{Mo}$  and  ${}^{90,96}\text{Nb}$ , and theoretical cross sections estimated from EMPIRE for the same residues at a given energy, respectively. A comparison has been made between the sum of measured cross sections from  $\alpha xn$  and  $pxn$  channels (i.e.,  $\sum \sigma_{\text{TF}}^{\alpha xn+pxn}$ ), theoretical predictions from EMPIRE (i.e.,  $\sum \sigma_{\text{theor}}^{\alpha xn+pxn}$ ), and ICF cross section (i.e.,  $\sigma_{\text{ICF}}$ ), as presented in Fig. 5(a).

It is evident from Fig. 5(a) that the relative separation between measured data (solid circles) and theoretical prediction on CF (solid triangles) increases with the gradual increase in projectile energy; it signifies that increasing bombarding energy fuels the breakup probability of weakly bound  ${}^7\text{Li}$ , a similar observation was reported earlier in the literature [20,23,24]. To measure the contribution of ICF over CF in  $\alpha$ - and  $p$ -emitting channels, and to understand its dependency on the incident energy, ICF strength fraction ( $F_{\text{ICF}}$ ) has been analyzed for the  ${}^7\text{Li}+{}^{\text{nat}}\text{Zr}$  system. The ICF strength fraction (%) is defined as  $F_{\text{ICF}} = (\sum \sigma_{\text{ICF}} / \sigma_{\text{TF}}^{\text{theor}})100$ , where  $\sigma_{\text{TF}}$  is the total theoretical fusion cross section (sum of all residual cross sections) anticipated from EMPIRE. Thus,  $F_{\text{ICF}}$  is not a purely measured quantity, rather it is a model-dependent fraction. The variation of  $F_{\text{ICF}}$  shows an increasing trend, between  $\approx 2$  and 10%, with growing bombarding energy, as presented

in Fig. 5(b). Hence, on average, a maximum of  $\approx 3\%$  ICF contribution up to 6.3 MeV/nucleon energy could be expected from each reaction channel.

In order to make a comparison between the  ${}^7\text{Li}$ -induced reactions on various targets, having mass  $\approx 90$ , and to blend the Coulomb barrier, a suitable data reduction method in energy has been adopted, as shown in Fig. 6. It depicts  $F_{\text{ICF}}$  as a function of reduced energy ( $E_{\text{c.m.}}/V_b$ ), which upholds a proportional relationship with incident energy. A similar trend of  $F_{\text{ICF}}$  has been observed from the  ${}^7\text{Li}$ -induced reactions on  ${}^{\text{nat}}\text{Mo}$ ,  ${}^{93}\text{Nb}$ ,  ${}^{89}\text{Y}$  [20,21,23], and  ${}^{\text{nat}}\text{Zr}$  (present work), as evident in Fig. 6. The ICF strength fraction for  ${}^7\text{Li}+{}^{\text{nat}}\text{Mo}$  is relatively higher as compared to other reactions, which might be due to some missing  $\alpha$ - and  $p$ -emitting channels in the  ${}^7\text{Li}+{}^{89}\text{Y}$ ,  ${}^7\text{Li}+{}^{\text{nat}}\text{Zr}$ , and  ${}^7\text{Li}+{}^{93}\text{Nb}$  reactions. It is worth mentioning here that Kumar *et al.* [20,21] observed five  $\alpha$ -emitting channels in  ${}^7\text{Li}+{}^{\text{nat}}\text{Mo}$  and one  $\alpha$  channel in  ${}^7\text{Li}+{}^{93}\text{Nb}$ , while three  $\alpha$ - and one  $p$ -emission channels were reported from  ${}^7\text{Li}+{}^{89}\text{Y}$  [23] to ICF. In the case of  ${}^7\text{Li}+{}^{\text{nat}}\text{Zr}$ , two  $\alpha$  channels and one  $p$  channel have been observed to contribute to the ICF strength fraction. On average,  $\approx 2$ –5% ICF per contributing channel has been observed from the above reactions up to  $\approx 6.5$  MeV/nucleon energy.

### C. Isomeric cross-section ratio

Nuclear isomers, highly excited metastable states, are the potential candidates to probe the structure of the nucleus, and this metastability of quantum states is distributed in neutron number, proton number, excitation energy, and angular momentum [62]. The isomeric nuclear pairs, which have the measurable half-lives, are used to predict the isomeric cross-section ratio (ICR), which yields the knowledge of  $\gamma$  de-excitation processes, transmutation of angular momentum, and couplings of different reaction channels. To characterize the relative population of the isomeric and ground states of  ${}^{93,95}\text{Tc}$  and to understand the effect of other factors like relative spins of the ground and isomeric states, projectile energy, types of emitted particles, level difference, and decay of compound nucleus, ICRs have been calculated for  ${}^{93m,g}\text{Tc}$  and  ${}^{95m,g}\text{Tc}$  pairs. ICR has been defined as the ratio of cross section of the isomeric state  $\sigma_m$  to the ground-state production cross section ( $\sigma_g$ ),  $\text{ICR} = \sigma_m / \sigma_g$ . The measured ICR values decreasing sharply with increasing  ${}^7\text{Li}$  energy in both cases, except for  ${}^{95}\text{Tc}$  beyond  $\approx 40$  MeV energy, where ICR becomes constant, as shown in Fig. 7. The observed trend of ICR could be understood as follows:  ${}^{93}\text{Tc}$  residues have ground-state spin  $9/2^+$  and isomeric state with spin  $1/2^-$  at 0.0- and 391.8-keV energies, respectively, while  ${}^{95}\text{Tc}$  has ground-state spin of  $9/2^+$  and isomeric state of  $1/2^-$  at 0.0 and 38.9 keV, respectively. The simplified decay schemes of  ${}^{93,95}\text{Tc}$  are shown in Figs. 8(a) and 8(b). The decay of the high-spin compound nucleus state is more probable to the high-spin ( $9/2^+$ ) state of the residue, which is ground state for both  ${}^{93}\text{Tc}$  and  ${}^{95}\text{Tc}$ , compared to the decay to  $1/2^+$  state; hence, a large population of those residues is observed in the ground state at low energies, leading to the sharp decrease in ICRs. However, as the incident energy increases, the high-energy state, having low spin ( $1/2^+$ ), starts populating; hence, a relatively slow fall



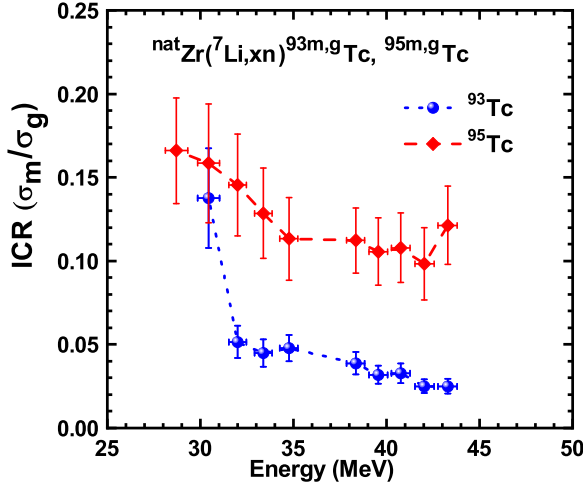


FIG. 7. Variation of ICRs of  ${}^{93}\text{Tc}$  and  ${}^{95}\text{Tc}$  is shown with projectile energies.

in the ICRs is observed, although the population of the ground state always stays high [63]. In the case of  ${}^{95}\text{Tc}$ , possibly an equilibrium between two spin states occurred above 40 MeV due to the release of large angular momentum through PEQ emissions from the composite system that led to almost constant ICRs, which also agrees with the trend reported in Ref. [64].

#### D. Coupled channel calculations and analysis

To assess the fusion cross section for  ${}^7\text{Li}+{}^{\text{nat}}\text{Zr}$  reaction within 28–44 MeV, coupled channel (CC) calculations have been performed using the modified version of the CCFULL code [65]. The code incorporates the inelastic couplings in the low-lying states of the projectile as well as the target. Although it allows a pair-transfer coupling between ground states of interacting nuclei, this degree of freedom has not been considered in the present calculation. The crucial part of its input parameter is the choice of nuclear potential for the estimation of fusion cross section; the Wood-Saxon form of nuclear potential with Akyuz-Winther (AW) parametrization has been adopted for the present calculations. The values of the parameters such as deformation parameter  $\beta$ , excitation energy  $E_x^*$  of considered excited states of interacting nuclei, and spin parity were taken from Refs. [5,6,8], and the calculated AW potential parameters are listed in Table IV. The weighted average of calculated AW potential parameters are  $V_0 = 44.2$  MeV,  $r_0 = 1.16$  fm, and  $a = 0.61$  fm. The AW potential parameters are slightly modified to fit the fusion barrier; values are  $V_0 = 48.0$  MeV,  $r_0 = 1.11$  fm, and  $a = 0.61$  fm. The parameters for the  ${}^{91}\text{Zr}$ , such as excitation energy of considered excited states of interacting partners and deformation parameter, have been calculated by taking the average of neighboring even-even isotopes ( ${}^{90}\text{Zr}$  and  ${}^{92}\text{Zr}$ ) following the reported prescription [9], since  ${}^{90}\text{Y}$  is an unstable neighboring nucleus. Full couplings in the ground state ( $3/2^-$ ) and the first excited state ( $1/2^-$ ) of the  ${}^7\text{Li}$  projectile and  $2^+$  and  $3^-$  vibrational states of the  ${}^{\text{nat}}\text{Zr}$  were incorporated in the calculation to figure out the coupling effect. Theoretical fusion

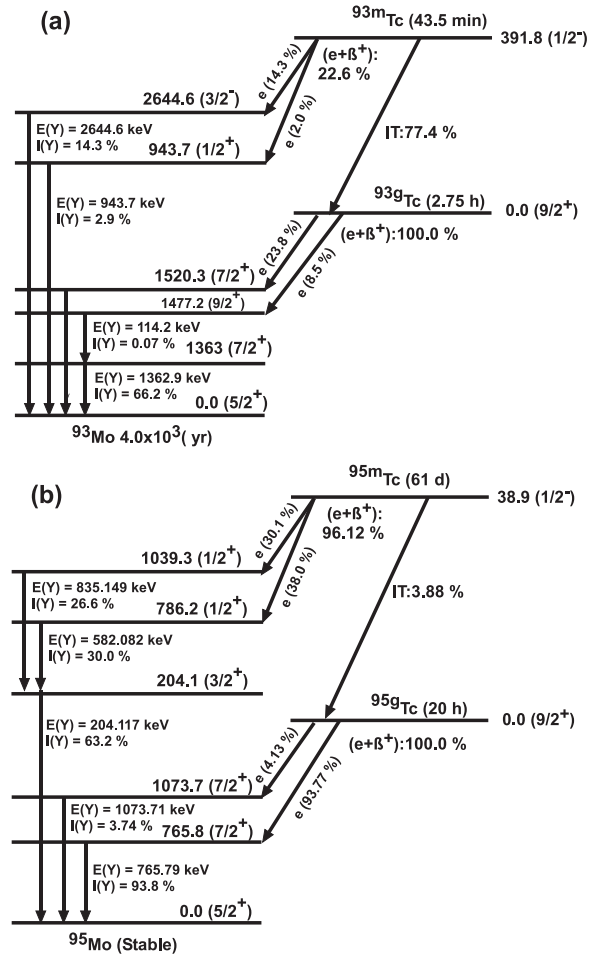


FIG. 8. Simplified decay scheme of isomeric pairs of (a)  ${}^{93}\text{Tc}$  and (b)  ${}^{95}\text{Tc}$ . Electron capture is denoted by  $e$ .

cross section for  ${}^7\text{Li}+{}^{\text{nat}}\text{Zr}$  system is the weighted average of all the naturally abundant isotopes of Zr.

The total fusion cross sections of  ${}^7\text{Li}+{}^{\text{nat}}\text{Zr}$  reaction from the CCFULL with and without couplings within the energy range considered, far above the Coulomb barrier energies, are

TABLE IV. List of the deformation parameters ( $\beta$ ), spin parity ( $J^\pi$ ), excitation energies of the states ( $E_x^*$ ), AW potential parameters, depth of the potential ( $V_0$ ), and diffuseness parameter  $a$  used in CC calculation for the  ${}^7\text{Li}+{}^{\text{nat}}\text{Zr}$  reaction.

Nucleus	$J^\pi$	$E_x^*$ (MeV)	$\beta$	System	$V_0$ (MeV)	$a$ (fm)
${}^{90}\text{Zr}$	$2^+$	2.19	0.089	${}^7\text{Li}+{}^{90}\text{Zr}$	44.22	0.612
	$3^-$	2.75	0.211			
${}^{91}\text{Zr}$	$2^+$	1.56	0.096	${}^7\text{Li}+{}^{91}\text{Zr}$	44.17	0.612
	$3^-$	2.54	0.192			
${}^{92}\text{Zr}$	$2^+$	0.93	0.103	${}^7\text{Li}+{}^{92}\text{Zr}$	44.12	0.613
	$3^-$	2.34	0.174			
${}^{94}\text{Zr}$	$2^+$	0.92	0.090	${}^7\text{Li}+{}^{94}\text{Zr}$	44.02	0.613
	$3^-$	2.06	0.193			
${}^{96}\text{Zr}$	$2^+$	1.75	0.080	${}^7\text{Li}+{}^{96}\text{Zr}$	43.93	0.613
	$3^-$	1.89	0.270			

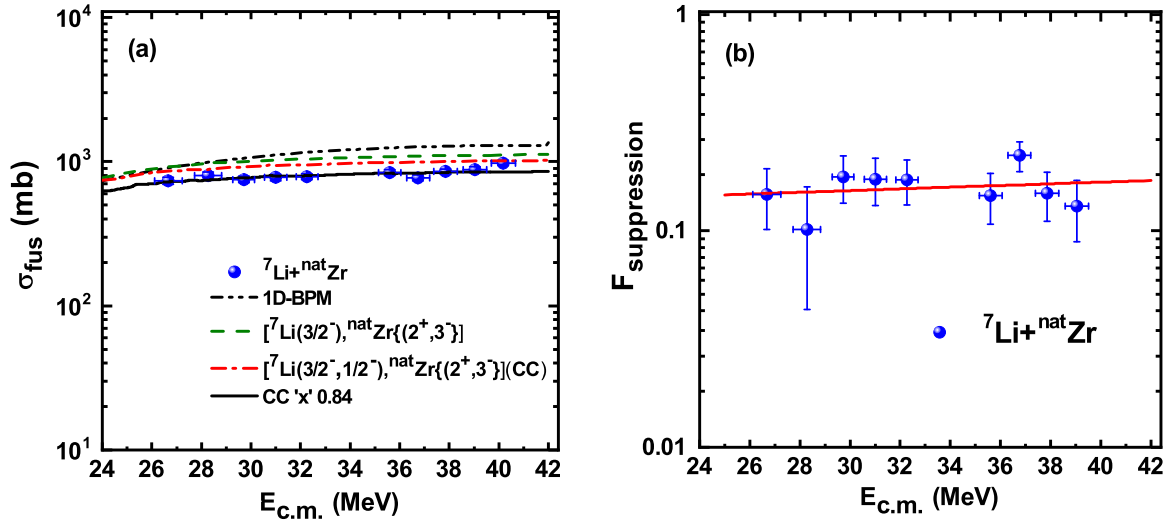


FIG. 9. (a) Comparison of measured fusion cross sections (circles) for  ${}^7\text{Li}+{}^{\text{nat}}\text{Zr}$  system and theoretical estimations from CCFULL with uncoupled (black dash-dotted line) and coupled (green dashed and red dash-dotted lines) levels; the solid line is for normalized  $\text{CC} \times 0.84$ , and (b) fusion suppression ( $F_{\text{suppression}}$ ) at energies far away from the Coulomb barrier in  ${}^7\text{Li}+{}^{\text{nat}}\text{Zr}$ ; the solid line represents a least-squares fit to the values.

higher than the experimental values as presented in Fig. 9(a). It can be observed that the measured cross sections, the sum of all residual cross sections at a given energy, are closer to the theoretical one when couplings are included in the ground as well as the first excited state of projectile and target (denoted as CC). Interestingly, the experimental data can be reproduced when the CC is multiplied by a factor of 0.84. Thus, it could be seen that the fusion cross section is  $\approx 16\%$  suppressed as compared to the CC estimate. Usually, a relative estimate of the fusion suppression at above-barrier energies depends on the below-barrier fusion cross sections, which are not measured in the present study. On the other hand, it is  $\approx 28\%$  suppressed as compared to the 1D BPM. The fusion suppression for  ${}^7\text{Li}+{}^{\text{nat}}\text{Zr}$  as a function of center-of-mass energy has been deduced and found to be almost constant over the energy range, as depicted in Fig. 9(b). The observed suppression in the fusion cross section of  ${}^7\text{Li}+{}^{\text{nat}}\text{Zr}$  might be due to the following reasons:

- (1) Due to the breakup of  ${}^7\text{Li}$ , some of the incident flux gets lost before interaction, and the breakup phenomena stay unaccounted for in the CCFULL calculation.
- (2) The residues which have short half-lives and the stable products (populated through  $xn$ ,  $pxn$ , and  $\alpha xn$  channels) could not be identified by the adopted technique.

In order to investigate the systematic of fusion suppression ( $F_{\text{suppression}}$ ) due to breakup of the projectile, a comparison has been made on the fusion suppression as a function of charge product of reaction ( $Z_p Z_T$ ) of weakly bound projectile  ${}^6,{}^7\text{Li}$ ,  ${}^9\text{Be}$ , and  ${}^{10}\text{B}$  mediated reactions in the medium to little-heavy mass targets, as shown in Fig. 10. The extents of suppression in the fusion cross section for  ${}^6\text{Li}$ -induced reactions on  ${}^{90,96}\text{Zr}$  [14,15] and  ${}^{144}\text{Sm}$  [7] were 34%, 25%, and 32%, respectively, while they were 16%, 24%, 25%, and 26% for  ${}^7\text{Li}+{}^{\text{nat}}\text{Zr}$  (present work),  ${}^7\text{Li}+{}^{144,154}\text{Sm}$  [8], and  ${}^7\text{Li}+{}^{159}\text{Tb}$  [16] reactions, respectively. Similarly, the CF suppressions

for  ${}^9\text{Be}+{}^{89}\text{Y}$  [9],  ${}^9\text{Be}+{}^{144}\text{Sm}$  [17], and  ${}^{10}\text{B}+{}^{159}\text{Tb}$  [16] were 20%, 10%, and 14%, respectively. All these reactions certainly do not follow the increasing trend in the suppression of the fusion cross section with the increasing charge of the target nuclei; a similar conclusion can be seen in Ref. [60]. Thus, it seems that the suppression of fusion is independent of the target nucleus charge, as also reported by Kumawat *et al.* [14] in many targets. Further, it has been found that fusion suppression is related to the  $\alpha$ -separation energy ( $S_\alpha$ ) of the projectile, and it increases with decreasing  $S_\alpha$ . As the  $\alpha$  breakup thresholds, which are 1.48, 2.45, 1.57, and 4.46 MeV for  ${}^6,{}^7\text{Li}$ ,  ${}^9\text{Be}$ , and  ${}^{10}\text{B}$ , respectively, of weakly bound projectiles increase, the suppression in the fusion cross section gets reduced (Fig. 10), as also pointed out in Refs. [7,60]. The

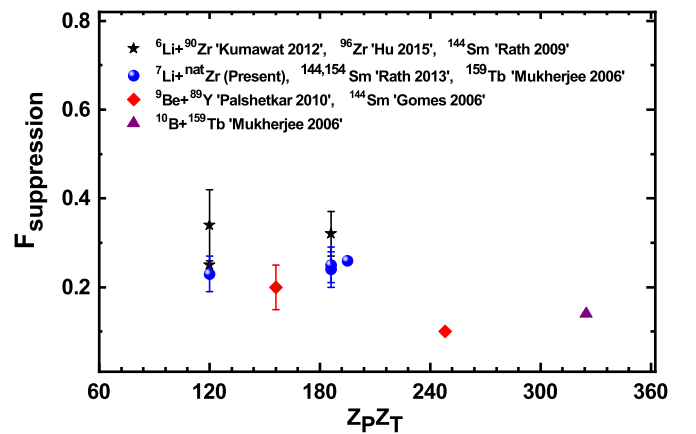


FIG. 10. Comparison of fusion suppression from the weakly bound projectile-induced ( ${}^6,{}^7\text{Li}$ ,  ${}^9\text{Be}$ , and  ${}^{10}\text{B}$ ) reactions on the medium and heavy mass targets such as  ${}^6\text{Li}+{}^{90}\text{Zr}$  [14],  ${}^6\text{Li}+{}^{96}\text{Zr}$  [15],  ${}^6\text{Li}+{}^{144}\text{Sm}$  [7],  ${}^7\text{Li}+{}^{\text{nat}}\text{Zr}$  (present study),  ${}^7\text{Li}+{}^{144,154}\text{Sm}$  [8],  ${}^7\text{Li}+{}^{159}\text{Tb}$  [16],  ${}^9\text{Be}+{}^{89}\text{Y}$  [9],  ${}^9\text{Be}+{}^{144}\text{Sm}$  [17], and  ${}^{10}\text{B}+{}^{159}\text{Tb}$  [16].

suppression in the fusion cross section was deduced from  $1 - \frac{\sigma_{\text{fus}}}{\sigma_{\text{CC}}}$ , where  $\sigma_{\text{fus}}$  is the experimentally measured fusion cross section and  $\sigma_{\text{CC}}$  is the coupled channel calculation predicted from CCFULL. Gomes *et al.* [28] also recalculated fusion suppression using the same expression for  $^9\text{Be}$  induced on different targets like  $^{89}\text{Y}$ ,  $^{124}\text{Sn}$ ,  $^{144}\text{Sm}$ , and  $^{208}\text{Pb}$  and observed that in some systems fusion suppression is independent of the charge of the target nucleus.

## V. CONCLUSION

In this article, we have measured the cross sections of product residues populated via the CF/ICF process in the  $^7\text{Li} + ^{\text{nat}}\text{Zr}$  reaction using the offline  $\gamma$ -ray technique within the 4.0 to 6.3 MeV/nucleon energy range. Comparison with theoretical Hauser-Feshbach formalism with EGSM level density for compound evaporation and exciton model for PEQ shows good agreement with the measured data that confirms the production of residues from the CF mechanism. However, the amount of enhancement observed in the  $\alpha$ - and

$p$ -emitting channels as compared to theoretical predictions could be attributed to the ICF of  $^7\text{Li}$ . It has been observed that the measured ICF strength fraction increases with the projectile energy. Comparison of fusion cross section with coupled channel calculation without the inclusion of breakup and transfer channels shows  $\approx 16\%$  suppression in the fusion of the  $^7\text{Li} + ^{\text{nat}}\text{Zr}$  reaction. It has also been observed that fusion suppression is independent of charge of the target nuclei and depends on  $\alpha$ -separation energies of loosely bound projectiles.

## ACKNOWLEDGMENTS

The authors thank the BARC-TIFR Pelletron team for their cooperation during the experiment and colleagues from the laboratory for their passionate teamwork during the experiment. Research Grant No. CRG/2018/002354 from SERB(IN), Grant No. 03(1467)/19/EMR-II from CSIR(IN), and the fellowship from MHRD, Government of India, are gratefully acknowledged.

- 
- [1] H. C. Britt and A. R. Quinton, *Phys. Rev.* **124**, 877 (1961).
- [2] Y. T. Oganessian, A. V. Yeremin, A. G. Popeko, S. L. Bogomolov, G. V. Buklanov, M. L. Chelnokov, V. I. Chepigin, B. N. Gikal, V. A. Gorshkov, G. G. Gulbekian *et al.*, *Nature (London)* **400**, 242 (1999), and reference therein.
- [3] J. J. Kolata, V. Guimarães, and E. F. Aguilera, *Eur. Phys. J. A* **52**, 123 (2016).
- [4] B. B. Back, H. Esbensen, C. L. Jiang, and K. E. Rehm, *Rev. Mod. Phys.* **86**, 317 (2014).
- [5] A. M. Stefanini, L. Corradi, A. M. Vinodkumar, Y. Feng, F. Scarlassara, G. Montagnoli, S. Beghini, and M. Bisogno, *Phys. Rev. C* **62**, 014601 (2000).
- [6] S. Kalkal, S. Mandal, N. Madhavan, E. Prasad, S. Verma, A. Jhingon, R. Sandal, S. Nath, J. Gehlot, B. R. Behera, M. Saxena, S. Goyal, D. Siwal, R. Garg, U. D. Pramanik, S. Kumar, T. Varughese, K. S. Golda, S. Muralithar, A. K. Sinha, and R. Singh, *Phys. Rev. C* **81**, 044610 (2010).
- [7] P. K. Rath, S. Santra, N. L. Singh, R. Tripathi, V. V. Parkar, B. K. Nayak, K. Mahata, R. Palit, S. Kumar, S. Mukherjee, S. Appannababu, and R. K. Choudhury, *Phys. Rev. C* **79**, 051601(R) (2009).
- [8] P. K. Rath, S. Santra, N. L. Singh, B. K. Nayak, K. Mahata, R. Palit, K. Ramachandran, S. K. Pandit, A. Parihari, A. Pal, S. Appannababu, S. K. Sharma, D. Patel, and S. Kailas, *Phys. Rev. C* **88**, 044617 (2013).
- [9] C. S. Palshetkar, S. Santra, A. Chatterjee, K. Ramachandran, S. Thakur, S. K. Pandit, K. Mahata, A. Shrivastava, V. V. Parkar, and V. Nanal, *Phys. Rev. C* **82**, 044608 (2010).
- [10] K. Hagino, A. Vitturi, C. H. Dasso, and S. M. Lenzi, *Phys. Rev. C* **61**, 037602 (2000).
- [11] L. F. Canto *et al.*, *Phys. Rep.* **424**, 1 (2006); **596**, 1 (2015).
- [12] I. Padron, P. R. S. Gomes, R. M. Anjos, J. Lubian, C. Muri, J. J. S. Alves, G. V. Martí, M. Ramírez, A. J. Pacheco, O. A. Capurro, J. O. F. Niello, J. E. Testoni, D. Abriola, and M. R. Spinella, *Phys. Rev. C* **66**, 044608 (2002).
- [13] R. M. Anjos, C. Muri, J. Lubian, P. R. S. Gomes, I. Padron, J. J. S. Alves, G. V. Martí, J. O. F. Niello, A. J. Pacheco, O. A. Capurro, D. Abriola, J. E. Testoni, M. Ramírez, R. Liguori Neto, and N. Added, *Phys. Lett. B* **534**, 45 (2002).
- [14] H. Kumawat, V. Jha, V. V. Parkar, B. J. Roy, S. K. Pandit, R. Palit, P. K. Rath, C. S. Palshetkar, S. K. Sharma, S. Thakur, A. K. Mohanty, A. Chatterjee, and S. Kailas, *Phys. Rev. C* **86**, 024607 (2012).
- [15] S. P. Hu, G. L. Zhang, J. C. Yang, H. Q. Zhang, P. R. S. Gomes, J. Lubian, X. G. Wu, J. Zhong, C. Y. He, Y. Zheng, C. B. Li, G. S. Li, W. W. Qu, F. Wang, L. Zheng, L. Yu, Q. M. Chen, P. W. Luo, H. W. Li, Y. H. Wu, W. K. Zhou, B. J. Zhu, and H. B. Sun, *Phys. Rev. C* **91**, 044619 (2015).
- [16] A. Mukherjee, S. Roy, M. K. Pradhan, M. S. Sarkar, P. Basu, B. Dasmahapatra, T. Bhattacharya, S. K. Basu, A. Chatterjee, V. Tripathi, and S. Kailash, *Phys. Lett. B* **636**, 91 (2006).
- [17] P. R. S. Gomes, I. Padron, E. Crema, O. A. Capurro, J. O. F. Niello, A. Arazi, G. V. Martí, J. Lubian, M. Trotta, A. J. Pacheco, J. E. Testoni, M. D. Rodríguez, M. E. Ortega, L. C. Chamon, R. M. Anjos, R. Veiga, M. Dasgupta, D. J. Hinde, and K. Hagino, *Phys. Rev. C* **73**, 064606 (2006).
- [18] M. Dasgupta, P. R. S. Gomes, D. J. Hinde, S. B. Moraes, R. M. Anjos, A. C. Berriman, R. D. Butt, N. Carlin, J. Lubian, C. R. Morton, J. O. Newton, and A. Szanto de Toledo, *Phys. Rev. C* **70**, 024606 (2004).
- [19] J. Lubian, T. Correa, B. Paes, J. M. Figueira, D. Abriola, J. O. F. Niello, A. Arazi, O. A. Capurro, E. de Barbará, G. V. Martí, D. M. Heinmann, A. E. Negri, A. J. Pacheco, I. Padron, and P. R. S. Gomes, *Nucl. Phys. A* **791**, 24 (2007).
- [20] D. Kumar, M. Maiti, and S. Lahiri, *Phys. Rev. C* **96**, 014617 (2017).
- [21] D. Kumar and M. Maiti, *Phys. Rev. C* **96**, 044624 (2017).
- [22] D. Kumar, M. Maiti, and S. Lahiri, *Phys. Rev. C* **94**, 044603 (2016).
- [23] R. Prajapat and M. Maiti, *Phys. Rev. C* **101**, 024608 (2020).
- [24] P. P. Singh, B. P. Singh, M. K. Sharma, Unnati, D. P. Singh, R. Prasad, R. Kumar, and K. S. Golda, *Phys. Rev. C* **77**, 014607 (2008).

- [25] L. R. Gasques, D. J. Hinde, M. Dasgupta, A. Mukherjee, and R. G. Thomas, *Phys. Rev. C* **79**, 034605 (2009).
- [26] D. Chattopadhyay, S. Santra, A. Pal, A. Kundu, K. Ramachandran, R. Tripathi, B. J. Roy, T. N. Nag, Y. Sawant, B. K. Nayak, A. Saxena, and S. Kailas, *Phys. Rev. C* **97**, 051601(R) (2018).
- [27] P. K. Giri, D. Singh, A. Mahato, S. B. Linda, H. Kumar, S. A. Tali, S. Parasari, A. Ali, M. A. Ansari, R. Dubey, R. Kumar, S. Muralithar, and R. P. Singh, *Phys. Rev. C* **100**, 024621 (2019).
- [28] P. R. S. Gomes, R. Linares, J. Lubian, C. C. Lopes, E. N. Cardozo, B. H. F. Pereira, and I. Padron, *Phys. Rev. C* **84**, 014615 (2011).
- [29] R. Rafiei, R. du Rietz, D. H. Luong, D. J. Hinde, M. Dasgupta, M. Evers, and A. Diaz-Torres, *Phys. Rev. C* **81**, 024601 (2010).
- [30] F. A. Souza, C. Beck, N. Carlin, N. Keeley, R. Liguori Neto, M. M. de Moura, M. G. Munhoz, M. G. Del Santo, A. A. P. Suaide, E. M. Szanto, and A. Szanto de Toledo, *Nucl. Phys. A* **821**, 36 (2009).
- [31] F. A. Souza, N. Carlin, C. Beck, N. Keeley, A. Diaz-Torres, R. Liguori Neto, C. Siqueira-Mello, M. M. de Moura, M. G. Munhoz, R. A. N. Oliveira, M. G. Del Santo, A. A. P. Suaide, E. M. Szanto, and A. Szanto de Toledo, *Eur. Phys. J. A* **44**, 181 (2010).
- [32] C. Beck, N. Rowley, P. Papka, S. Courtin, M. Rousseau, F. A. Souza, N. Carlin, R. Liguori Neto, M. M. de Moura, M. G. Del Santo, A. A. P. Suaide, M. G. Munhoz, E. M. Szanto, A. Szanto de Toledo, N. Keeley, A. Diaz-Torres, and K. Hagino, *Nucl. Phys. A* **834**, 440c (2010).
- [33] F. A. Souza, N. Carlin, C. Beck, N. Keeley, A. Diaz-Torres, R. Liguori Neto, C. Siqueira-Mello, M. M. de Moura, M. G. Munhoz, R. A. N. Oliveira, M. G. Del Santo, A. A. P. Suaide, E. M. Szanto, and A. Szanto de Toledo, *Nucl. Phys. A* **834**, 420c (2010).
- [34] C. Beck, N. Keeley, and A. Diaz-Torres, *Phys. Rev. C* **75**, 054605 (2007).
- [35] S. K. Pandit, A. Shrivastava, K. Mahata, V. V. Parkar, N. Keeley, P. C. Rout, K. Ramachandran, C. S. Palshetkar, I. Martel, A. Kumar, A. Chatterjee, and S. Kailas, *Phys. Rev. C* **100**, 014618 (2019).
- [36] S. K. Pandit, A. Shrivastava, K. Mahata, N. Keeley, V. V. Parkar, P. C. Rout, K. Ramachandran, I. Martel, C. S. Palshetkar, A. Kumar, A. Chatterjee, and S. Kailas, *Phys. Rev. C* **93**, 061602(R) (2016).
- [37] A. Shrivastava, A. Navin, N. Keeley, K. Mahata, K. Ramachandran, V. Nanal, V. V. Parkar, A. Chatterjee, and S. Kailas, *Phys. Lett. B* **633**, 463 (2006).
- [38] D. Kumar and M. Maiti, *Phys. Rev. C* **95**, 064602 (2017).
- [39] R. Prajapat, M. Maiti, D. Kumar, and A. Chauhan, *Phys. Scr.* **95**, 055306 (2020).
- [40] M. Maiti and S. Lahiri, *Phys. Rev. C* **84**, 067601 (2011).
- [41] M. Maiti, *Phys. Rev. C* **84**, 044615 (2011).
- [42] M. Maiti and S. Lahiri, *Phys. Rev. C* **81**, 024603 (2010).
- [43] D. Kumar, M. Maiti, and S. Lahiri, *Sep. Sci. Technol.* **52**, 2372 (2017).
- [44] M. Maiti and S. Lahiri, *Radiochim. Acta* **99**, 359 (2011).
- [45] M. Maiti and S. Lahiri, *Radiochim. Acta* **103**, 7 (2015).
- [46] M. Maiti, *Radiochim. Acta* **101**, 437 (2013).
- [47] A. Chauhan, M. Maiti, and S. Lahiri, *Phys. Rev. C* **99**, 064609 (2019).
- [48] J. F. Ziegler, M. D. Ziegler, and J. P. Biersack, *Nucl. Instrum. Methods Phys. Res. B* **268**, 1818 (2010).
- [49] B. Wilken and T. A. Fritz, *Nucl. Instrum. Methods* **138**, 331 (1976).
- [50] J. Kemmer and R. Hofmann, *Nucl. Instrum. Methods* **176**, 543 (1980).
- [51] M. Herman, R. Capote, B. V. Carlson, P. Obložinský, M. Sin, A. Trkov, H. Wienke, and V. Zerkin, *Nucl. Data Sheets* **108**, 2655 (2007).
- [52] J. Raynal, Optical-model and coupled-channel calculations in nuclear physics, International Atomic Energy Agency Report IAEA-SMR-9/8, 1972, <http://inspirehep.net/record/19572/files/sti-pub-306.pdf#page=291>.
- [53] C. H. Dasso and S. Landowne, *Comput. Phys. Commun.* **46**, 187 (1987).
- [54] T. Tamura, T. Udagawa, and H. Lenske, *Phys. Rev. C* **26**, 379 (1982).
- [55] H. Nishioka, J. J. M. Verbaarschot, H. A. Weidenmüller, and S. Yoshida, *Ann. Phys.* **172**, 67 (1986).
- [56] R. Capote, M. Herman, P. Obložinský, P. G. Young, S. Goriely, T. Belgia, A. V. Ignatyuk, A. J. Koning, S. Hilaire, V. A. Plujko, M. Avrigeanu, O. Bersillon, M. B. Chadwick, T. Fukahori, Z. Ge, Y. Han, S. Kailas, J. Kopecky, V. M. Maslov, G. Reffo, M. Sin, E. S. Soukhovitskii, and P. Talou, *Nucl. Data Sheets* **110**, 3107 (2009).
- [57] A. Gilbert and A. G. W. Cameron, *Can. J. Phys.* **43**, 1446 (1965).
- [58] A. V. Ignatyuk, J. L. Weil, S. Raman, and S. Kahane, *Phys. Rev. C* **47**, 1504 (1993).
- [59] A. D'Arrigo, G. Giardina, M. Herman, A. V. Ignatyuk, and A. Taccone, *J. Phys. G* **20**, 365 (1994).
- [60] V. Jha, V. V. Parkar, and S. Kailas, *Phys. Rep.* **845**, 1 (2020)
- [61] National Nuclear Data Center, Brookhaven National Laboratory [<http://www.nndc.bnl.gov/nudat2/>].
- [62] P. Walker and G. Dracoulis, *Nature (London)* **399**, 35 (1999).
- [63] A. Chauhan and M. Maiti, *Phys. Rev. C* **99**, 034608 (2019).
- [64] S. Mukherjee, N. L. Singh, G. K. Kumar, and L. Chaturvedi, *Phys. Rev. C* **72**, 014609 (2005).
- [65] K. Hagino, N. Rowley, and A. T. Kruppa, *Comput. Phys. Commun.* **123**, 143 (1999).